

Boosting oxygen activation in ceria-oxide via gallium addition

T.A. Zepeda^{a,*}, R. Ponce-Pérez^a, A. Solis-Garcia^a, J. Guerrero-Sánchez^a, S. Fuentes^a,
S.A. Gómez^b

^a Universidad Nacional Autónoma de México, Centro de Nanociencias y Nanotecnología, Carretera Tijuana, Ensenada km 107, Ensenada, B.C. 22800, Mexico

^b Departamento de Ingeniería de Procesos e Hidráulica, Universidad Autónoma Metropolitana-Iztapalapa, Av. San Rafael Atlixco No. 186, Col. Vicentina, Ciudad de México 09340, Mexico

ARTICLE INFO

Keywords:
Cerium oxide
Gallium oxide
CO oxidation
Operando FTIR
Oxygen activation, Oxygen vacancies

ABSTRACT

CeO₂ is a well-suited support due to its higher oxygen storage capacity and reversible redox ability, which is associated with the oxygen activation. Herein we report the effective oxygen activation in CeO₂ by gallium incorporation, varying the Ga/Ce molar ratios from 0.25 to 0.75. Structural results and operando spectroscopies under reaction conditions revealed that gallium incorporation improves the oxygen activation in CeO₂, being more effective at low gallium content (Ga/Ce of 0.25). Atomic-scale computations demonstrated that the 0.25 Ga/Ce molar ratio generates Ga atomic-size channels that allow an easy way for oxygen diffusion from bulk to the surface. Ga incorporates into the subsurface Ce layer causing a collective effect: weakening the surface Ce-O bonds, boosting the surface oxygen activation, then enhancing the CO oxidation ability. Once this happens, it leaves behind O-vacancies, which may occupy either bulk oxygen from the CeO₂ or further renovation of oxygen atoms from the environment.

1. Introduction

Industrial development and the growing use of automobiles for transportation have increased the demand for fossil fuels, which has caused a drastic increase in atmospheric pollution [1]. Carbon monoxide (CO) stands out since it is a highly toxic gas, causing severe health consequences and irreparable ecological damage [2,3]. Therefore, searching for strategies to reduce atmospheric CO concentration is an urgent task that attracts numerous focused research groups. One of the principal strategies to reduce CO emissions from the incomplete combustion of fossil fuels in automobiles is its oxidation to CO₂ through catalytic converters [4,5].

Due to their high activity, noble metals (Pt, Rh, and Pd) have been widely used as catalysts for CO oxidation [6–9]. These metals are generally supported on zeolites, SiO₂, ZrO₂, Al₂O₃, TiO₂, and CeO₂ to increase their dispersion [10–15]. Among these oxides, the cerium oxide is a well-suited as support due to its higher oxygen storage capacity (OSC) compared to other metal oxides. This property has been associated with the facile change between reduced and oxidized states (Ce³⁺ ↔ Ce⁴⁺) through their rapid and reversible ability to uptake and release oxygen [16,17], playing an essential role in three-way catalysts [4,6,10,15].

The OSC is classified into total and dynamic [18]; the latter is the most important for catalytic oxidation reactions (as CO oxidation) because it is related to the donation of available oxygen atoms, even at low temperatures [18]. Nevertheless, the oxygen supply could decrease considerably due to strongly adsorbed carbonate species on the ceria surface, derived from CO₂ adsorption formed during CO oxidation [19]. J. Vecchietti et al. [20,21], found that gallium-doped cerium oxide inhibits the formation of surface carbonates. Also, the redox properties and oxygen mobility were improved compared to the bare CeO₂.

The high OSC of cerium oxide is also attributed to the presence of oxygen vacancies on its surface [22]. These vacancies are believed to play a vital role in facilitating the adsorption and activation of oxygen. These characteristics make cerium oxide an excellent support for synthesizing catalysts for various oxidation reactions, including CO removal via oxidation [22,23].

Furthermore, the oxygen vacancies on the cerium oxide surface have been demonstrated to significantly contribute to catalytic activity by providing sites for the adsorption and activation of reactant molecules [22].

In recent years, numerous studies have focused on investigating the mechanisms underlying the role of oxygen vacancies in cerium oxide. The insights gained from these investigations have not only advanced

* Corresponding author.

E-mail address: trino@ens.cnyn.unam.mx (T.A. Zepeda).



our understanding of the fundamental aspects but also have implications for the development of highly active and selective catalysts for CO oxidation [22,23].

Ga-doping has also been used in CeO₂-based catalysts to engineer their catalytic properties. For example, it was suggested that Ga doping in Pt/CeO₂ single-atom catalysts facilitates oxygen vacancy creation to enhance the CO oxidation reaction [24]. This fact was corroborated by density functional theory calculations in which the energy barrier for vacancy formation is lower when adding Ga to the catalyst [24]. S. Tang et al. [25] reported Ga doping in Pd/CeO₂ single-atom catalysts also enhances the catalytic activity for CO oxidation, in which employs density functional theory (DFT) calculations and transition state theory to systematically investigate the impact of Ga atom doping on the catalytic performance. Remarkably, DFT calculations reveal that the stability of Pd single atoms supported on the CeO₂ (111) surface is significantly enhanced by Ga doping. An oxygen vacancy, generated easily near the Ga and Pd site, serves a critical function in activating the adsorbed oxygen molecule. Most importantly, the authors demonstrate that Ga doping considerably reduces the highest energy barrier during the CO oxidation reaction, implying that the catalytic performance of the CO oxidation reaction is effectively promoted [25].

Furthermore, Ga-doping on Pt/CeO₂-Al₂O₃ catalysts enhances propylene desorption as a product of propane dehydrogenation [26]. The Ga-doping in CeO₂ has applications in the ethanol steam reforming reaction, in which the H₂:CO₂ ratio is improved due to Ga impurities [27].

Based on the information described above, in this work, ceria-gallium oxides were synthesized by the coprecipitation method to evaluate the Ga effect in the catalysis of CO oxidation developed over CeO₂. Details such as the reducibility, oxygen activation, inhibition of the surface carbonates species formation, and oxygen vacancies in the samples were obtained by a combined study of the redox properties and catalytic performance under operando conditions. Theoretical calculations were carried out to understand, at the atomic scale, the oxygen vacancy formation and the O diffusion improvements related to Ga content. Results demonstrate that Ga incorporation generates atomic-size channels, facilitating the O atom diffusion to reach the surface and further react with CO. The difference in electronegativity between Ga and Ce -when Ga replaces Ce atoms- weakens the Ga-O bonds improving the O vacancies formation. This behavior is also seen at the surface, where the O atoms near the incorporated Ga atom will be the ones that improve the CO oxidation. Electron localization function evidence that Ga atoms do not accumulate charge allowing easy CO₂ desorption after reaction and reducing the formation of surface carbonate species.

2. Experimental

2.1. Synthesis of the oxides

The bare ceria, bare gallium, and gallium-cerium oxides, varying the Ga/Ce molar ratio of 0.25, 0.50, and 0.75, were prepared by the precipitation method. A detailed description of the oxides synthesis is presented in the *Supplementary Information (SI) (Section 1)*. The labeling of the samples were 0.25GaCe, 0.50GaCe and 0.75GaCe for the Ga/Ce molar ratio of 0.25, 0.50, and 0.75, respectively. An additional gallium-impregnated ceria oxide sample was prepared for comparison. This sample was prepared by the incipient wet impregnation method, with Ga loading similar to that of the sample with a Ga/Ce atomic ratio of 0.25, which was labeled as 0.25GaCe-IMP.

2.2. Catalysts characterization

Textural properties were recorded with a Micromeritics TriStar 3000 apparatus at -196 °C. X-ray diffraction (XRD) patterns were recorded a step size of 0.021°/min, from 10° to 80° (2θ) in a PANalytical Aeris diffractometer using an radiation soured of Cu Kα ($\lambda = 1.5405 \text{ \AA}$). The

UV-vis diffuse reflectance spectroscopy (DRS) were recorded using a Agilent Cary-5000 UV-Vis spectrophotometer equipped with an integrating sphere. Temperature-programmed reduction (H₂-TPR) of the samples was carried out in a homemade system equipped with a thermal conductivity detector. Prior to the TPR characterizations, 30 mg of sample was degassed at 150 °C in N₂ flow for 1 h, they were cooled down to room temperature, then the flow was changes to 25 ML/min of 10 %H₂/Ar mixture gas, then the TPR measurements were performed, at a heating rate of 10 °C/min. The oxygen storage capacity (OSC) was calculated from H₂-TPR profiles.

2.3. CO oxidation procedure

2.3.1. CO oxidation reaction procedure

The oxidation of CO was performed in a homemade fixed-bed flow reactor at atmospheric pressure. 30 mg of sample, with a grain size of 0.2–0.3 mm, was placed on a tubular quartz micro-reactor ($\phi = 12.6 \text{ mm}$) with a porous quartz frit in the middle. Before the CO oxidation procedure, samples were calcined in situ from room temperature up to 400 °C, at a heating rate of 10 °C/min for 1.5 h with a flow of 60 ML/min of O₂/N₂ mixture (5 % O₂ vol/vol). The gas feed stream was 1 % CO, 0.5 % O₂, and He as the balance gas, reaching a contact time W/F_{CO} = 40 g_{cat} h mol_{CO}⁻¹. The reactor was connected online to a gas chromatograph (Shimadzu 12-A) equipped with a thermal conductivity detector, using both 5 Å and Porapack Q packed columns.

2.3.2. Temperature-dependent CO oxidation in the absence of oxygen

The oxidation of CO in the absence of oxygen was evaluated by determining CO consumption as a function of temperature calculated through TPR-CO profiles. A gas mixture containing 1.0 vol% CO and helium balance was introduced to the catalyst sample (60 mg) at a flow rate of 40 cm³min⁻¹, while the temperature was varied from ambient to 400 °C at a heating rate of 5 °C/min. The concentrations of CO and CO₂ were measured during the experiment. Before each TPR-CO test, the catalysts were pretreated with a 20 % O₂/He gas mixture at 400 °C for 2 h, followed by cooling under the same mixture to ambient temperature. The samples were then purged to remove residual oxygen and physisorbed species under a flow of 100 cm³min⁻¹ for 1 h. It is essential to note that high-purity gases were used, and the gas mixture was passed through a homemade trap to capture any potential traces of residual oxygen.

2.4. Operando spectroscopy studies

2.4.1. Operando DRS UV-vis study under reaction conditions

DRS UV-vis spectra during CO oxidation were recorded using a CARY/5E Agilent spectrophotometer equipped with a diffuse reflectance reaction cell (Harrick Scientific), using a reaction mixture gas CO/O₂/N₂ with molar ratio of 1/0.5/98.5, a contact time W/F_{CO} = 40 g_{cat} h mol_{CO}⁻¹, and a heating rate of 2 °C/min. A detailed description is presented in the *SI (Section 2)*.

2.4.2. Operando FTIR study under reaction conditions

Operando FTIR spectra were carried out in an Agilent 660 spectrophotometer equipped with an ISRI transmission flow reactor/cell with CaF₂ windows, using a reaction mixture gas flow of CO/O₂/N₂ with molar ratio of 1/0.5/98.5, a contact time W/F_{CO} = 40 g_{cat} h mol_{CO}⁻¹, and a heating rate of 2 °C/min. A detailed description is presented in the *SI (Section 3)*.

2.5. Density-functional theory (DFT) calculations

We performed first-principles calculations based on the periodic Density Functional Theory as implemented in the *Vienna Ab-initio Simulation Package* (VASP) [28–31] to investigate the Ga role on the CO oxidation reaction. Electronic states were expanded in plane waves

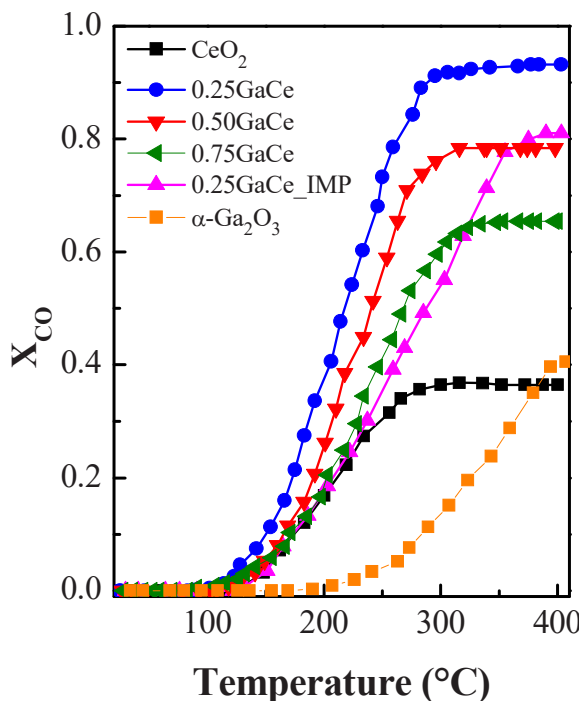


Fig. 1. CO conversion as a function of the temperature over isotherms of the Ga-containing CeO_2 samples. For comparison, a sample with the same gallium loading as the 0.25GaCe sample was included, which was prepared by the wet impregnation method (0.25GaCe-IMP). Reaction mixture: 1 % CO, 0.5 % O_2 , 98.5 % N_2 , contact time W/FCO = 40 g_{cat} h molCO⁻¹.

with an energy cutoff of 450 eV. The electron-ion interaction was treated employing the pseudopotential method with PAW pseudopotentials [32, 33]. The exchange-correlation energies consider the generalized gradient approximation (GGA) with PBE parametrization [34]. Van der Waals interactions have been accounted for by employing the D3 correction method of Grimme et al. [35,36]. We used the supercell method to simulate the gallium-cerium oxides at 0.25, 0.50, and 0.75 in a $2 \times 2 \times 1$ supercell; such supercell size is appropriate to treat such Ga contents. In the geometry optimization, convergence is achieved when all force components are less than 0.01 eV/Å and the energy differences are less than 1×10^{-4} eV as in previous reports [37–39]. Brillouin zone was sampled with an equally spaced k-points mesh in a $6 \times 6 \times 6$ grid for the unit cell [40]. In the Supporting Information (Section 4), we provide details on the computational parameter optimization considered in this work. The Climbing Image Nudged Elastic Band (CI-NEB) method is employed to analyze oxygen diffusion [41,42]. Seven intermediate images were considered from the initial to final stages.

3. Results and discussions

3.1. Catalytic activity in the CO Oxidation reaction

The results of CO conversion over the oxides are shown in Fig. 1. For comparison, the oxidation of CO on Ga-impregnated CeO_2 , with Ga/Ce molar ratios from 0.25 was included. The bare CeO_2 and Ga_2O_3 oxides have poor activity compared to the other studied samples. The bare CeO_2 oxide reaching their maximum conversion (36 % of conversion) at 285 °C, while the bare Ga_2O_3 oxide reaches its maximum conversion (41 % conversion) at 400 °C. Ga-containing samples showed higher activity for CO oxidation compared to bare oxides. The higher Ga loading sample (0.75GaCe) displayed similar activity to the bare CeO_2 sample up to around 200 °C, above this temperature a gradual increment in the CO oxidation as a function of the temperature is observed, reaching its maximum conversion (65 % of conversion) at 330 °C. The samples with

Table 1

Textural properties and CeO_2 lattice constant of the Ga-containing CeO_2 oxides.

Sample	S_{BET} (m^2/g)	V_p (cm^3/g)	D_p (nm)	Size crystal (nm)	$a^0 \text{CeO}_2 a$ (Å)
CeO_2	91	0.129	5.5	8.8	5.41
0.25 GaCe	104	0.136	4.7	4.4	5.36
0.50 GaCe	74	0.078	4.1	3.6	5.37
0.75 GaCe	88	0.087	4.0	3.3	5.38
$\alpha\text{-Ga}_2\text{O}_3$	55	0.101	6.1	15.3	-

^a calculated from refinement of the diffraction patterns on the most intense peak of CeO_2 support ($25^\circ < 2\theta < 30^\circ$), corrected with the graphite peak around 26.5° , using the $a_0 = \sqrt{(h^2 + k^2 + l^2)} \left(\frac{\lambda}{2 \sin \theta} \right)$ equation.

lower Ga-content (0.25GaCe and 0.50GaCe) displayed superior catalytic behavior. The 0.25GaCe sample reached 93 % of CO conversion at 290 °C, while the 0.50GaCe sample achieves 79 % of CO conversion at 310 °C.

There is an improvement in the activity during the oxidation of CO due to the incorporation of gallium. In that sense, to obtain more details about the effect of gallium on the activity during CO oxidation, a sample with similar Ga loading to the more active sample (0.25GaCe) was prepared by the wet impregnation method (0.25GaCe-IMP) and evaluated under the same conditions. The 0.25GaCe-IMP sample displayed a similar performance to the bare CeO_2 in the activity for CO oxidation until approximately 230 °C; above this temperature, the CO conversion increases as temperature function, reaching a maximum CO conversion (80 %) at 380 °C. This behavior was lower than the catalytic performance observed on the 0.25GaCe sample.

These findings indicate that the method used for incorporating gallium into cerium-gallium oxide samples may have an impact on their catalytic performance during CO oxidation.

3.2. Characterization of the oxides

Table 1 shows the textural properties of the samples. The N_2 adsorption-desorption isotherms (Fig. S2), are type IV in the IUPAC classification [43]. The bare gallium oxide sample had a S_{BET} value of $55 \text{ m}^2 \text{ g}^{-1}$, while the bare CeO_2 sample shows an S_{BET} of $91 \text{ m}^2 \text{ g}^{-1}$. Incorporating low gallium content (0.25GaCe) increases the surface area value to $104 \text{ m}^2 \text{ g}^{-1}$. As the gallium content rises, the surface area decreases considerably, displaying a lower S_{BET} value for the 0.50GaCe sample ($74 \text{ m}^2 \text{ g}^{-1}$). In contrast, the S_{BET} value for the 0.75GaCe sample is very close to the S_{BET} value of bare CeO_2 .

The behavior observed in the surface area values was similar to V_p values. The bare CeO_2 sample shows a higher D_p value than the other samples. The D_p decreases gradually as a function of gallium loading.

XRD patterns are shown in Fig. S3. The XRD pattern of the bare CeO_2 sample displays characteristic peaks of the fluorite phase from the ceria oxide, while the XRD pattern of the bare Ga_2O_3 sample shows characteristic peaks of the alpha phase of the gallium oxide [43]. All mixed Ce-Ga oxides samples showed reflection peaks associated with the ceria oxide fluorite phase [44,45]. No reflection peaks characteristic to gallium oxide particles were detected on the mixed oxides, suggesting that gallium could be included into of the crystallographic cell of CeO_2 .

The crystal size was calculated using the Scherrer equation (Table 1). The bare CeO_2 material displayed a crystal size value of 8.8 nm, which was decrease gradual as a function of the gallium content (Table 1). The crystal size for the crystalline lattice of CeO_2 follows the order: bare CeO_2 (8.8 nm) > 0.25GaCe (4.4 nm) > 0.50GaCe (3.6 nm) > 0.75GaCe (3.3 nm).

Lattice constant parameters displayed a slight contraction of the CeO_2 lattice, as consequence of the Ga incorporation (Table 1). The 0.25GaCe sample displays the lowest CeO_2 lattice constant among the

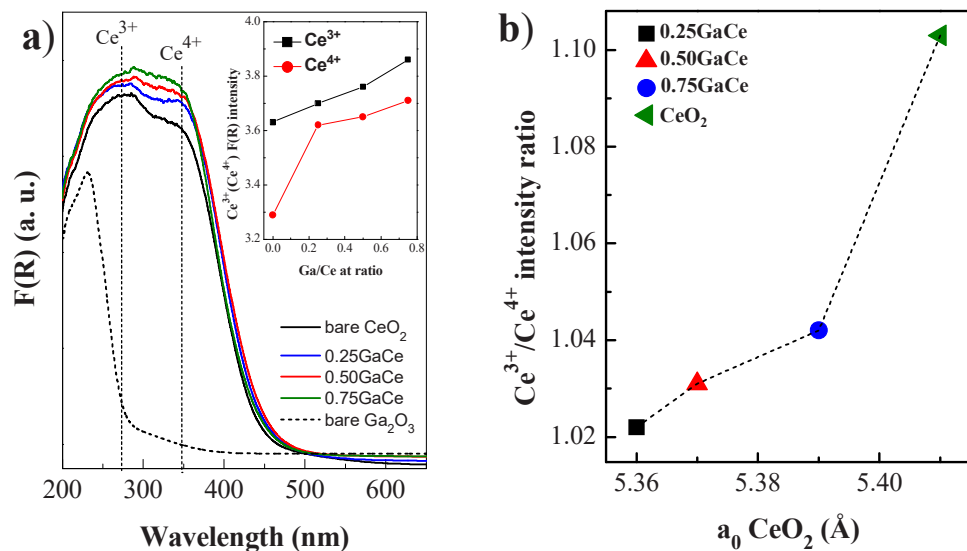


Fig. 2. a) DRS UV-vis of the Ga-containing CeO₂ oxides and the evolution of the intensity of the Ce³⁺ and Ce⁴⁺ species with respect to the gallium content (shown in insert); b) correlation between the intensity Ce³⁺/Ce⁴⁺ ratio regard to the lattice constant (a^0) of CeO₂ (data Table 1).

samples, to higher gallium content the lattice constant parameter was increase as a function of gallium loading. The CeO₂ lattice constant follows the order: bare CeO₂ (5.41 Å) > 0.75GaCe (5.39 Å) > 0.50GaCe (5.37 Å) > 0.25GaCe (5.36 Å). J.L. da Silva [46], reported a DFT investigation on the energetics, structural properties and oxygen-deficient of CeO₂ and CeO_{1.5} phases. The authors found that, the Ce atoms change the oxidation state from Ce⁴⁺ in CeO₂ phase to Ce³⁺ species in the oxygen-deficient CeO_{1.5} phase, which led to a change in the expansion of the cell volume in the CeO₂ phase, due to a change in the size of the Ce⁴⁺ atoms from 0.97 Å to 1.14 Å for the Ce³⁺ species. The CeO₂ volume expansion due to a reduction of ceria atoms from Ce⁴⁺ to Ce³⁺ has been reported by several authors [47–50].

The lattice constant values shown in Table 1, suggest that gallium addition leads to important changes in the electronic environment of the ceria atoms. The oxidation of the ceria atoms from Ce³⁺ to Ce⁴⁺ ions being promoted by gallium might induce a contraction of the CeO₂ volume, because of a smaller ionic size of the Ce⁴⁺ species. To clarify this, the electronic changes of Ce^{δ+} species was investigated using DRS-UV technique. Fig. 2a shows the DRS-UV spectra for the Ga-containing CeO₂ and the evolution of the intensity of the Ce³⁺ and Ce⁴⁺ species with respect to the gallium content (shown in the inset). Fig. 2b shows a correlation of the intensity of the Ce³⁺/Ce⁴⁺ ratio as a function of the lattice constant (a^0) of CeO₂ (Table 1).

The spectrum of the bare gallium oxide shows a strong absorption band at 246 nm, which is close to that of pure α-Ga₂O₃ oxide [51]. The ceria-containing oxides showed two intense bands at 270 and 345 nm, which were assigned to Ce³⁺ and Ce⁴⁺ species, respectively [43,50,52]. The intensity of the absorption bands of both Ce³⁺ and Ce⁴⁺ species, were changed by the incorporation of gallium (inset Fig. 2a). The higher intensity Ce³⁺/Ce⁴⁺ ratio value was observed on the bare CeO₂ sample (1.103). The value of this ratio decreased drastically for the sample with the lowest gallium loading (0.25GaCe sample), subsequently, this intensity gradually increases as a function of gallium content (inset Fig. 2a). The intensity Ce³⁺/Ce⁴⁺ ratio follows the order: bare CeO₂ (1.103) > 0.75GaCe (1.042) > 0.50GaCe (1.031) > 0.25GaCe (1.022). This means that the presence of gallium ions promoted the oxidation of Ce³⁺ to Ce⁴⁺ ions.

We found a interesting correlation between the intensity Ce³⁺/Ce⁴⁺ ratio as a function of the lattice constant (a^0) of CeO₂ (Fig. 2b). This means that while a contraction of the volume of lattice CeO₂ oxide occurs, the fraction of ceria atoms with coordination Ce⁴⁺ increases, due to the oxidation from Ce³⁺ to Ce⁴⁺, then the gallium incorporation induced

Table 2

Dynamic oxygen storage capacity (OSC) and total H₂ consumption during TPR of samples.

Sample	Total H ₂ Consumption (μmol H ₂ /g)	Dynamic OSC ^a (μmol O/g)	
		(< 200 °C)	(> 200 < 450 °C)
CeO ₂	315.1	-	132.1
0.25GaCe	518.5	7.2	335.1
0.50GaCe	462.7	4.3	272.6
0.75GaCe	416.3	2.1	231.2
0.25GaCe -IMP	447.4	0.4	150.2

^a Dynamic OSC was determined from TPR profiles

the oxidation Ce³⁺to Ce⁴⁺ ions, consequence, a contraction of the lattice constant was observed.

H₂-TPR results for the Ga-containing CeO₂ oxides are shown in Fig. S4. The H₂-TPR profile for the Ga impregnated on CeO₂ sample, with similar gallium loading to the 0.25GaCe sample, was included for comparison. The reduction profile for the bare α-Ga₂O₃ oxide (Fig. S4f) shows a strong peak at 558 °C, which is close to the reduction of bulk α-Ga₂O₃ oxide [53]. The bare CeO₂ sample shows three reduction peaks characteristic of ceria oxide, centered at 340, 420, and 685 °C (Fig. S4a). Peaks at 340 and 420 °C correspond to oxygen withdrawal from the surface (corresponding to the reduction of surface Ce⁴⁺ species) [54–56], while the reduction peak at 730 °C corresponds to oxygen stored in the ceria bulk [56–58].

H₂-TPR profiles for the Ga-incorporated samples have a similar shape to the bare CeO₂ sample (Fig. S4b-d). The temperature reduction peaks characteristic to the CeO₂ reduction remain at about the same temperature for all samples, although it shows an important increase in the H₂ consumption in the lower temperature reduction peaks (340 and 420 °C) concerning the bare CeO₂ sample. Furthermore, the higher temperature reduction peak (685 °C) shows a slight decrease in the H₂ consumption with respect to the CeO₂ sample (Table 2), mainly for low gallium loadings, indicating an improved removal of oxygen from the CeO₂ bulk. This was the opposite for the gallium-impregnated sample (Fig. S4e), in which the H₂ consumption decreased noticeably for the lower temperature reduction peaks (340 and 420 °C), while the H₂ consumption was greater in the higher temperature reduction peak (Table 2).

Notably, the gallium-containing samples present a reduction peak at

558 °C, linked to the reduction of bulk α -Ga₂O₃ oxide [53]. The H₂ consumption for this reduction peak increases gradually as a gallium function (Table 2). As expected, the reduction of gallium oxide species was very noticeable in the gallium-containing sample prepared by the impregnation method. Interestingly, the mixed oxides samples (Ga_(x)Ce) show a reduction peak at low temperatures between 180 and 195 °C, which was shifted in temperature on the medium and higher gallium loading. The reduction peak at low temperatures was not observed on the sample prepared by the impregnation method. This reduction peak can be attributed to an activation of surface oxygen at low temperatures caused by gallium incorporation.

It is probable that in the 0.25GaCe-IMP sample, gallium is predominantly present on the surface due to the conditions of the impregnation method (as the H₂-TPR results suggest, Fig. S4). Nevertheless, the possibility that a portion of Ga could also be incorporated into the lattice cannot be ruled out. This may account for the increase in CO production compared to the pure oxides, as well as its lower CO generation than the 0.25GaCe sample, which is prepared by the co-precipitation method and has a higher distribution of Ce and Ga within the lattice of the material. This assessment could clarify the differences between samples prepared via impregnation and those prepared using the co-precipitation method.

3.3. Ga effect on the oxygen activation in ceria oxide during the CO oxidation

3.3.1. Role of dynamic OSC in CO oxidation

To obtain information about the effect of gallium addition into the CeO₂ lattice on the redox properties of the Ce ions, the oxygen storage capacity (OSC) of the oxides was measured through H₂-TPR profiles [18, 21, 46]. The OSC is classified into two categories: (i) thermodynamic or total OSC, which considers the overall amount of transferable oxygen (surface and bulk oxygen), and (ii) dynamic OSC, which reflects the most reactive oxygen species, involving mainly the surface oxygen and oxygen vacancies, which it is related to the surface mobility of oxygen [18, 59].

The dynamic OSC values calculated considered two temperature regions, the first up to 200 °C and the second at temperatures between 200 and 450 °C (Table 2). The gallium content samples showed higher dynamic OSC values than bare CeO₂ oxide. Interestingly, adding gallium to the ceria lattice enables oxygen activation at temperatures below 200 °C. The largest OSC value was observed in the 0.25GaCe sample. As the gallium content increases in the mixed oxides, the dynamic OSC value decreases as a function of gallium loaded. In contrast, the dynamic OSC value for the impregnated gallium sample (0.25GaCe-IMP) was slightly higher than the bare CeO₂ sample. The sequence of the dynamic OSC values in the temperature interval from 200° to 450°C was 0.25GaCe (335.1 μmol O/g) > 0.50GaCe (272.6 μmol O/g) > 0.75GaCe (231.2 μmol O/g) > bare CeO₂ (132.1 μmol O/g). This trend is also valid for the dynamic OSC values observed below 200 °C. Surface oxygen mobility at low temperatures (>200 °C) should strongly impact the catalysis of the samples in the CO oxidation.

It has been reported that CeO₂ oxide reduction is enhanced by gallium addition since it improves the CeO₂ reducibility because Ga-OH species are involved in the surface reduction of ceria atoms from Ce⁴⁺ to Ce³⁺ [20, 21]. This agrees with our H₂-TPR results and with the observed dynamic OSC values. Ga addition drastically improves the dynamic OSC in the CeO₂ oxide, indicating an increase in the number of surface and/or subsurface reducible Ce⁴⁺ ions, which are transferred from the bulk [43], as well as was observed by DRS UV-vis results.

A linear relationship between the ignition temperatures in the CO oxidation taken at 50 % of conversion (T-CO_{50%}) and the total dynamic OSC (10–450 °C) of the gallium-containing samples exist, which reached T-CO_{50%} values, as shown in Fig. S5. Where it is possible to observe that regardless of the gallium incorporation method (precipitation or impregnation), the T-CO_{50%} values decrease with the increase of the dynamic surface oxygen, indicating that this property (activated

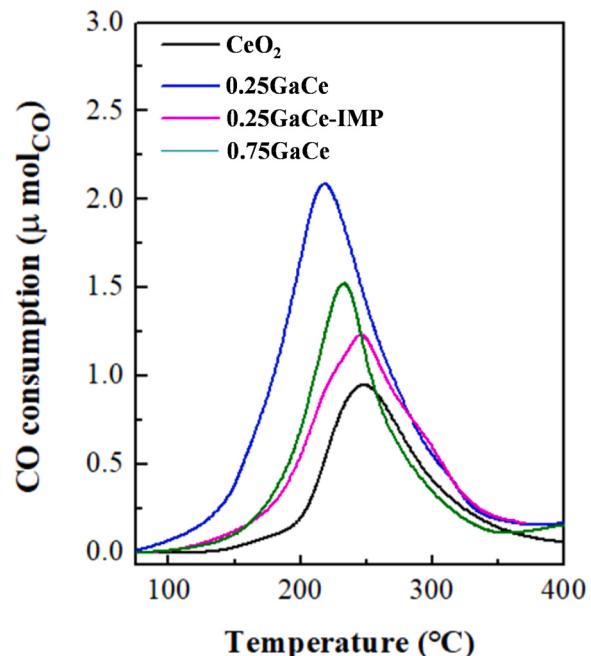


Fig. 3. CO consumption as a temperature dependence during the TPR-CO profiles over bare CeO₂, 0.25GaCe, 0.25GaCe-IMP and 0.75GaCe samples.

on the surface) directly influences the CO oxidation. Similarly, Bueno-López et al. [60] reported that the dynamic oxygen of CeO₂ is more important than the bulk oxygen for oxidation reactions. These results can indicate that the gallium addition to the ceria lattice enhances the number of the most reactive surface oxygen species; even oxygen activation was observed at low temperatures (below 200 °C), which is crucial in the oxidation reactions [61–65], specifically in CO oxidation [64, 65].

CO oxidation, conducted in the absence of oxygen and as a function of temperature, can be evaluated through TPR-CO profiles. These results provide insights into the oxygen activation on the CeO₂ lattice facilitated by the addition of gallium. CO consumption as a temperature dependence during the TPR-CO profiles for the selected samples are presented in Fig. 3. The CO consumption over bare CeO₂ support increases with temperature until a maximum of 250 °C (reached 0.94 μmol_{CO}). This is due to the consumption of the available surface oxygen. The presence of gallium species enabled surface oxygen mobility, observing the highest CO consumption on the 0.25GaCe sample in the temperature range studied. This sample reaches a CO consumption of 2.17 μmol_{CO} at 210 °C. Towards higher gallium contents (0.75GaCe), the CO consumption decreased, and the temperature of the maximum conversion increased (225 °C).

The CO consumption on the gallium-impregnated sample (0.25GaCe) displayed a performance similar to the bare CeO₂ sample. These results agree with the dynamic OSC. Therefore, we can conclude that the presence of gallium in the CeO₂ lattice improves the oxygen supply of the surface towards the CO oxidation, as represented schematically in Fig. S6. The gallium incorporation boosts the mobility and activation of the surface oxygen atoms for the oxidation of CO to CO₂; simultaneously, the reduction of the surface Ce⁴⁺ ions to Ce³⁺ ions occur.

3.3.2. Operando DRS UV-vis study under reaction conditions

To understand the oxygen activation of the samples, we measured operando DRS UV-vis spectra at the same reaction conditions described in the catalytic evaluation section. Figs. 4a and 4b shown the electronic spectra under operando conditions during CO oxidation on the bare CeO₂ and 0.25GaCe samples, respectively. The evolution of the Ce³⁺/

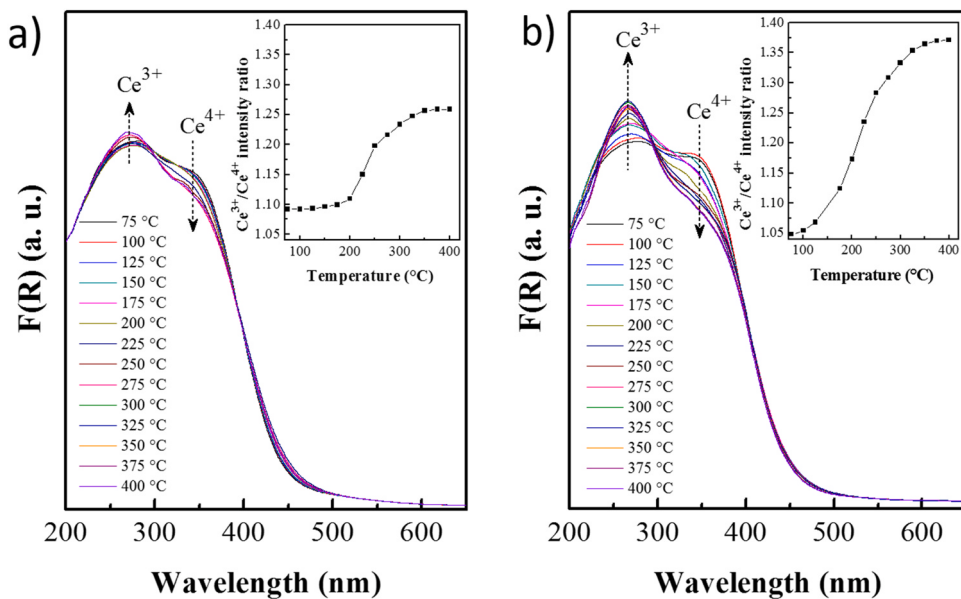


Fig. 4. DRS UV-vis spectra during the CO conversion as a function of the temperature over the a) bare CeO₂ and b) 0.25GaCe samples. Reaction mixture: 1 % CO, 0.5 % O₂, 98.5 % N₂, contact time W/FCO = 36 g_{cat} h molCO⁻¹.

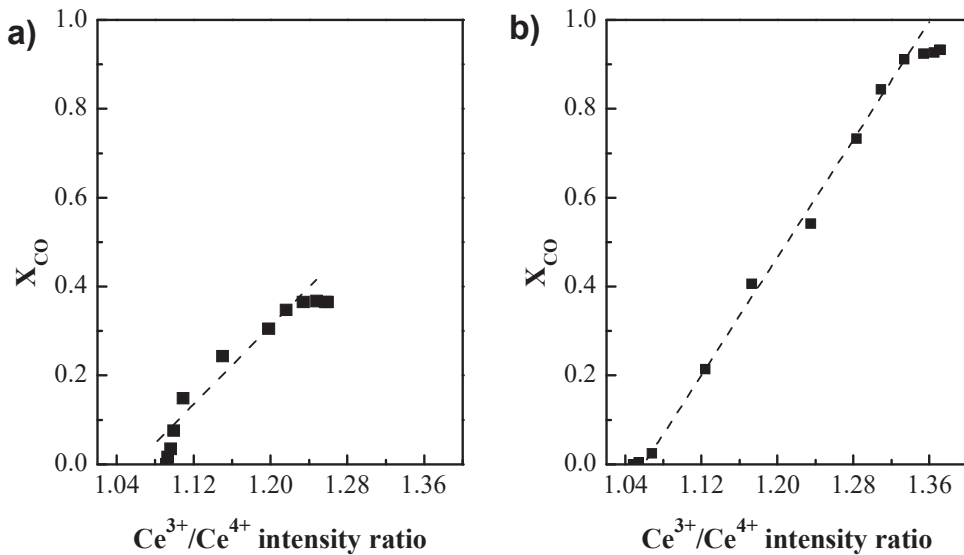


Fig. 5. Correlation of the fraction of CO converted (X_{CO} from Fig. 1) as a function of the evolution of the intensity Ce³⁺/Ce⁴⁺ ratio under operation conditions (From Figs. 10 and 10) over a) bare CeO₂ and b) 0.25GaCe samples.

Ce⁴⁺ ratio intensity as a function of the temperature is depicted in the inset of the same figure. DRS UV-vis spectra during CO oxidation of both samples showed two intense absorption bands in the charge transference region located at 270 and 345 nm, which are associated with Ce³⁺ and Ce⁴⁺ species, respectively [24,50,52].

The intensity Ce³⁺/Ce⁴⁺ ratio remained closed on the bare CeO₂ sample from room temperature to 175 °C (Fig. 4a). Above this temperature, a light decrease in ceria Ce⁴⁺ species as a function of the temperature was observed; simultaneously, an increase in the intensity signal corresponding to the Ce³⁺ species occurs, as consequence, the value intensity Ce³⁺/Ce⁴⁺ ratio increased, reaching a higher intensity ratio at around 300 °C (Fig. 4a). After this temperature, the value of this ratio remained constant. Our results suggest that the ceria ions are reduced from Ce⁴⁺ to Ce³⁺ during the CO oxidation reaction.

The changes in the electronic environment of the ceria atoms were more noticeable for the 0.25GaCe sample, in contrast to the bare CeO₂

sample. A drastic increase in the intensity associated with Ce³⁺ species as function of the temperature was observed on the spectra corresponds to the 0.25GaCe sample (Fig. 4b). At the same time, a noticeable decrease in the intensity band related to Ce⁴⁺ species was observed (Fig. 4b). The intensity Ce³⁺/Ce⁴⁺ ratio began to increase below 100 °C, achieving the maximum increase to 350 °C. Above this temperature, the value of this ratio remained constant.

Gallium incorporation induced important changes in the electronic environment of the ceria ions under reaction conditions. The increment of the intensity Ce³⁺/Ce⁴⁺ ratio during the reaction progress is related to the formation of oxygen vacancies, which leads to further reduction of active O_x species [21].

The behavior of the intensity Ce³⁺/Ce⁴⁺ ratio versus temperature (insets in Fig. 4) is similar to the CO conversion curve (Fig. 1). Figs. 5a and 5b show a correlation of the X_{CO} as a function Ce³⁺/Ce⁴⁺ ratio evolution intensity under operation conditions over bare CeO₂ and

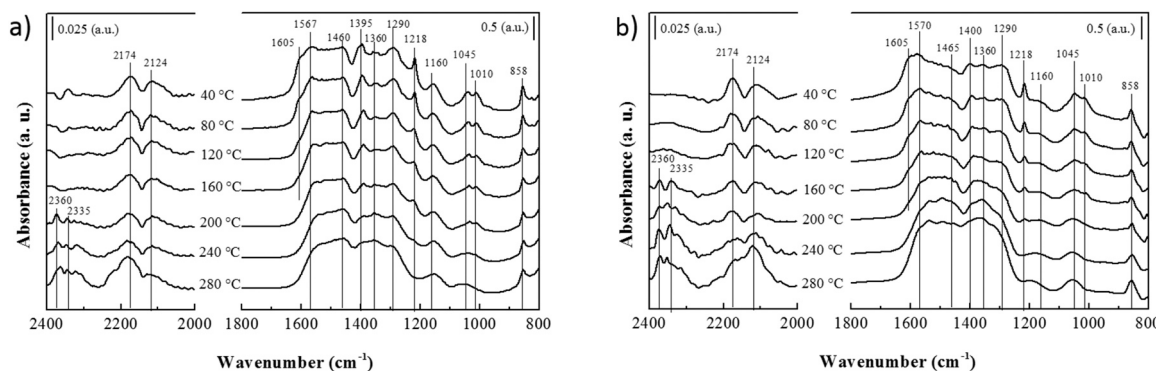


Fig. 6. FTIR characterization of CeO₂ sample recorded during the flow of the reactive mixture (1 % CO, 0.5 % O₂, 98.5 % N₂) at increasing temperature. Contact time W/FCO = 36 g_{cat} h molCO⁻¹. The FTIR spectrum before reaction was subtracted from the FTIR spectra collected under reaction conditions.

0.25GaCe samples, respectively.

J. Vecchietti et al. [21], studied the surface reduction mechanism of cerium–gallium mixed oxides experimentally and through calculations by density functional theory. The reported results showed that the gallium-doped ceria oxides are more reducible than the bare CeO₂. The authors found that an energy of 3.23 eV is necessary to form an oxygen vacancy in the bare CeO₂ sample. In comparison, only 2.54 eV is needed to create an oxygen vacancy in the cerium–gallium mixed oxides with a molar composition of 0.25GaCe. The highlighted results were that the presence of gallium strongly modifies the local environment of the lattice ceria ions, and the gallium sites are located in tetrahedral coordination instead of cubic in the fluorite structure. When the oxygen atom is removed, the gallium atoms are in a relaxation phenomenon; then, the gallium atom binds to another oxygen behind, so the lattice compensates for the absence of an oxygen atom. This ability may be the cause of a facility to the reduction-reoxidation process. Besides, they reported that only Ce⁴⁺ species are reduced to Ce³⁺ species, while the Ga³⁺ species remain fully oxidized at temperatures up to 400 °C. These conclusions agree with our results, which clearly show that the gallium-doped oxides are more reducible, and the mobility and activation of surface oxygen under reaction conditions were higher than the bare CeO₂ sample.

3.3.3. Operando FTIR study under reaction conditions

Figs. 6a and 6b show the infrared spectra recorded during the flow of the reactive mixture (1 % CO, 0.5 % O₂, 98.5 % N₂) over bare CeO₂ and 0.25GaCe samples respectively. At 40 °C, several bands emerged after the contact of the reactive mixture with the bare cerium oxide. The bands at 1605, 1395, and 1045 cm⁻¹ can be associated with ν(CO₃) vibration modes of surface bicarbonate species (Fig. 6a) [66–69]. The presence of these species is reinforced by the bands observed at 1218 and 858 cm⁻¹, which can be attributed to δ(OH) and π(CO₃) of bicarbonate species (Fig. 6a) [66–69]. The bands located at 1567, 1290, and 1010 cm⁻¹ can be assigned to the stretching of CO₃ of bidentate carbonate on CeO₂ [54–57]. Additionally, two bands at 1460 and 1360 cm⁻¹ are observed in Fig. 6; these can be due to monodentate carbonate species (ν(CO₃)) [66–69].

In the CO stretching region, two bands were detected at 2174 and 2124 cm⁻¹. They can be attributed to CO bonded to Ce⁴⁺ and Ce³⁺ ions, respectively [66–69]. Once the temperature increased, the bands of CO bonded to Ce⁴⁺ and Ce³⁺ sites decreased gradually until 200 °C (Fig. 6a and S7a). As these bands decreased in intensity, new adsorption bands were not observed until 200 °C. Then, the decrease in the intensity of the bands at 2174 and 2124 cm⁻¹ might be related to the thermal desorption of CO as a function of the temperature. At temperatures above 200 °C, two new bands were observed at 2360 and 2325 cm⁻¹, attributed to gas phase CO₂. Then, the intensity of these bands increased as a temperature function (Fig. 6a). The increment in the CO_{2(g)} formation matches with the increase in the intensity of the bands of CO adsorbed on Ce⁴⁺ and Ce³⁺ sites. Therefore, it is assumed that both species are

participating in the catalysis of CO oxidation. The bicarbonate and carbonate species bands in the bidentate configuration decreased along the experiment as the temperature increased (Figs. 6a and S7b), probably caused by the thermal desorption of CO of these species. Regarding carbonate species, in monodentate configuration, it is observed that they stayed approximately constant during the CO oxidation. Our results suggest Ce⁴⁺ and Ce³⁺ sites are the main surface intermediates during CO oxidation.

Fig. 6b shows the FTIR characterization of the 0.25GaCe sample during the CO oxidation. Similar bands were observed in the IR spectra of the 0.25GaCe sample. At 40 °C bands of CO on Ce⁴⁺ and Ce³⁺ sites were observed at 2174 and 2124 cm⁻¹, respectively. Also, IR signals of bicarbonate species (1605, 1395, 1218, 1045, and 858 cm⁻¹), carbonate species in bidentate species (1570 or 1567, 1290 and 1010 cm⁻¹), and monodentate configuration were observed (Fig. 6b) [66–69].

The bands of CO on Ce⁴⁺ and Ce³⁺ sites in the 0.25GaCe sample showed a similar behavior compared to the bare CeO₂ sample. They decreased their intensity gradually until 200 °C (Figs. 6b and S8a). As previously mentioned, the decrease in its intensity is related to the thermal desorption of CO on these sites. Above this temperature, their intensities increased as a temperature function. In parallel, bands related to CO_{2(g)} (2360 and 2325 cm⁻¹) appeared from 160 °C; their intensity increases drastically with the temperature.

From both behaviors, it is possible to assume that the CO adsorbed on Ceⁿ⁺ sites participates in the transformation of CO to CO_{2(g)}. The evolution of the bands of carbonaceous species (Fig. S8a) revealed that the species bicarbonate and bidentate carbonate decreased progressively between 40 and 200 °C, possibly due to thermal desorption of CO. Above 200 °C, these two surface species incremented their intensity, which is consistent with the production of CO_{2(g)}. Hence, the formation of these species could be related to CO_{2(g)} re-adsorption. The bands of monodentate carbonate increased during CO oxidation, as observed in Figs. 6b and S8b. Therefore, we conclude that these species are accumulated on the surface of the 0.25GaCe, and probably do not participate in the CO oxidation.

3.4. Atomistic description of Ga effect on the electronic environment of CeO₂

To corroborate that Ga occupies the Ce sites in the CeO₂ compound, we performed a thermodynamic analysis through DFT calculations considering the substitution of Ce by Ga, O by Ga, and interstitial Ga atoms. Since a different number of atoms and chemical species were considered, we employed the Defect Formation Energy (DFE) formalism [38,70–72], which only depends on the chemical potential, and it helps explain the relative stability of structures at different growth conditions. Such formalism can be adapted to our system as:

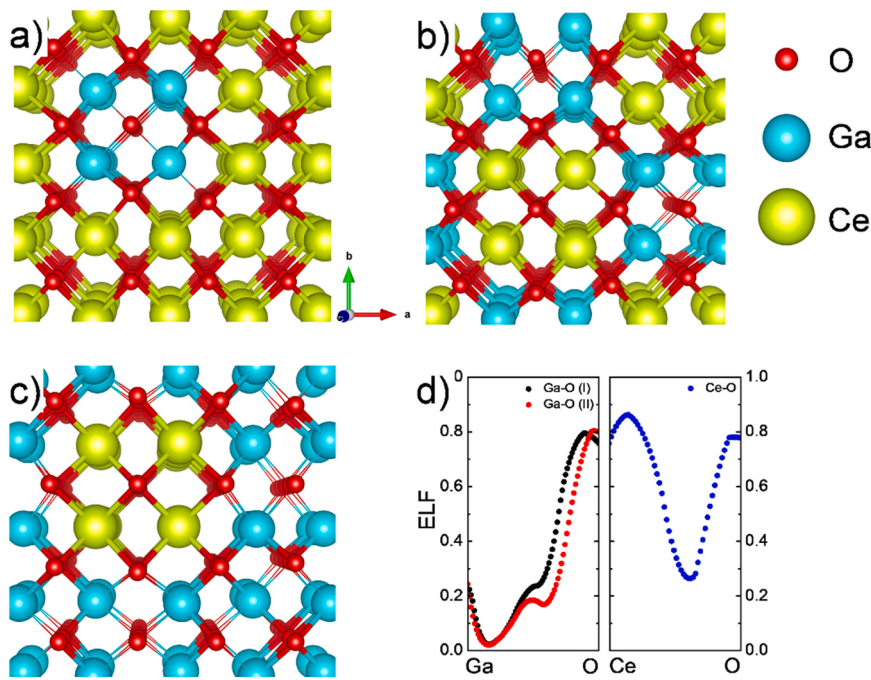


Fig. 7. Atomistic models for the a) 0.25GaCe, b) 0.50GaCe, and c) 0.75GaCe. Thinner sticks represent Ga-O interactions, d) ELF line profiles for the bonds present in the systems.

Table 3

Structural parameters and bond distances for the pristine CeO₂, 0.25GaCe, 0.50GaCe and 0.75GaCe.

System	Cell parameter (Å)	Bond distance (Å)		
		Ce-O	Ga-O (I)	Ga-O (II)
CeO ₂	5.44	2.36		
0.25GaCe	5.34	2.34	2.13	2.27
0.50GaCe	5.21	2.33	2.12	2.30
0.75GaCe	5.06	2.32	2.11	2.26

$$E^{DFE} = \frac{1}{V} \left(E^{\text{slab}} - \mu_{\text{Ce}} \left(n_{\text{Ce}} - \frac{n_O}{2} \right) - \frac{\mu_{\text{CeO}_2} n_O}{2} - \mu_{\text{Ga}} n_{\text{Ga}} \right) \quad (1)$$

where V is the volume of the unit cell or the surface area -it depends if we are working with bulks or surfaces-, E^{slab} is the total energy of the system at hand, n_i is the number of atoms of the ith species and μ_i is the chemical potential. We vary the chemical potential for Ce from Ce-rich to Ce-poor conditions. Also, μ_{Ga} varies from Ga-rich to Ga-poor conditions. With this, a three-dimensional plot is generated, where, according to our formalism, the most stable models are those which provide the lowest energy values. We also project the 3D plot into a 2D phase diagram where the chemical regions are well-defined for each thermodynamically stable structure.

The results for bulk structure are shown in Fig. S9a. Notice that the bare CeO₂ (blue color) is the most stable structure at almost all the chemical potential regions, except at Ga-rich, Ce-poor conditions, where the substitution of Ce by Ga stabilizes (red color). Similar behavior is noticed for the (111) surface (Fig. S9b). In this case, the oxygen-terminated bare CeO₂ (111) surface (blue color) is stable for almost the entire region of chemical potential, and the substitution of Ce by Ga (red color) is stable at Ce-poor, Ga-rich conditions and Ga-poor, Ce-poor conditions, just as in the bulk case.

Our calculations agree with the XRD patterns demonstrating that Ga occupies Ce sites, and no secondary stable structures are observed. Fig. S9c displays the atomistic model of the CeO₂ bulk structure, which according to our calculations, it has lattice parameter a = 5.44 Å, in good agreement with our experiment. Each Ce atom interacts with eight

neighboring oxygen atoms, each with a bond distance of 2.36 Å.

Furthermore, when Ga is placed in the Ce sites, two different bonds can be distinguished: the Ga-O (I) with a bond distance of 2.13 Å and the Ga-O (II) with a bond distance of 2.27 Å. Once we demonstrate that Ga occupies the Ce sites, the supercell method with a 2 × 2 × 1 periodicity is employed to simulate the 0.25GaCe, 0.50GaCe, and 0.75GaCe stoichiometries. Atomistic models for each concentration are depicted in Fig. 7.

Table 3 summarizes the cell parameters and bond distances for each system. For the 0.25GaCe system, the lattice constant gets contracted by 1.83 % (a = 5.34 Å), from a = 5.44 Å to a = 5.34 Å. Similar behavior is observed for 0.50GaCe and 0.75GaCe systems, where the lattice parameter contracts by 4.22 % and 6.98 %, respectively. This effect is directly related to the difference in atomic radius between Ce and Ga. The theoretical cell parameter corresponding to the CeO₂ and 0.25GaCe samples are very close to those estimated experimentally (Table 1).

However, the experimental cell parameters for the 0.50GaCe and 0.75GaCe samples increased slightly (Table 1). In contrast, the theoretical values decreased as a function of gallium loading (Table 3). We consider these results valid and comparable since there may be experimental factors such as vacancies not being considered in the theoretical estimates. Also, as Ga content increases, the bond distances contract. These are: 2.34 Å, 2.33 Å, and 2.32 Å for 0.25GaCe, 0.50GaCe, and 0.75GaCe, respectively. Similar behavior is observed for the Ga-O(I) bonds, with values 2.13 Å, 2.12 Å, and 2.11 Å for 0.25GaCe, 0.50GaCe, and 0.75GaCe, respectively. Fig. 7a, b and c correspond to the 0.25GaCe, 0.50GaCe, and 0.75GaCe models, respectively. In these figures, Ga-O(I) interactions are represented by thicker sticks, and the Ga-O (II) are the thinner ones. For the 0.25GaCe and 0.50GaCe models, notice that Ga tends to occupy Ce sites around an O atom in tetrahedral coordination composed of Ga-O (II) interactions, forming atomic-size channels. Such channels may facilitate the O(II) diffusion towards the surface to achieve CO oxidation. For 0.25GaCe, the number of Ga-O (I) and (II) are the same, while for 0.50GaCe, 75 % of the Ga-O interactions are of type (I) and 25 % of type (II), this behavior explains the Ga-O (II) bonds elongation in the 0.50GaCe system (see Table 3).

The electron localization function (ELF) was calculated to elucidate the nature of the interactions in the systems, see Fig. 7d. The Ce-O

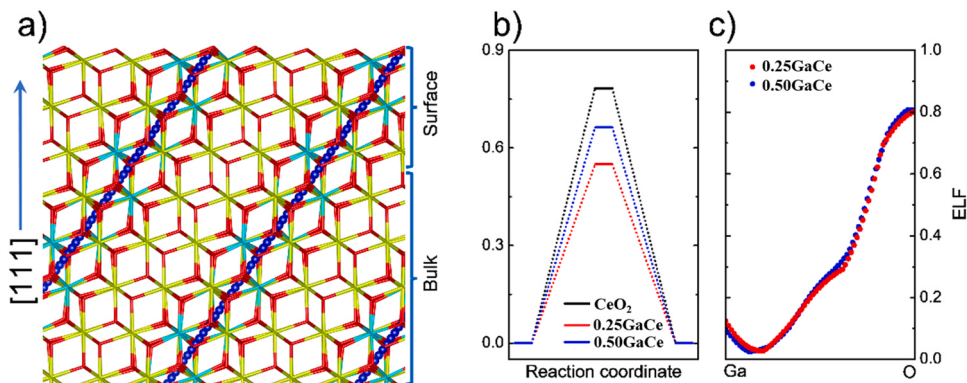


Fig. 8. Atomistic scheme of the oxygen diffusion (blue spheres) from bulk to the surface, b) energy barriers for the oxygen diffusion in the CeO₂, 0.25GaCe and 0.50GaCe systems, c) ELF line profile for the middle point of the O diffusion for the 0.25GaCe and 0.50GaCe systems.

interaction (blue dotted line) shows an ionic behavior, while the Ga-O interactions have a similar trend. However, the ELF line profiles show less electron population around the Ga-O bond than Ce-O, suggesting that Ga-O bonds are weaker. Also, the Ga-O (II) (red dotted line) has less electron population than Ga-O (I) (black dotted line), denoting an even weaker bond. From this analysis, we can conclude that O atoms in the Ga-O (II) sites can easily diffuse to the surface thanks to the weak interaction with Ga and the formation of above mentioned atomic-size channels.

To corroborate our assumptions, we perform CI-NEB calculations to evaluate the O diffusion into the bare CeO₂, 0.25GaCe, and 0.50GaCe. In all cases, the initial and final states correspond to the ideal O position in the crystal. The oxygen diffusion is simulated by moving the O to a neighboring equivalent position. In systems with Ga, diffusion is carried out by moving the O atoms with Ga tetrahedral coordination to an equivalent position. Fig. 8a depicts the atomic-size diffusion channels from the bulk toward the surface. Results from the O(II) diffusion are depicted in Fig. 8b. O diffusion in the bare CeO₂ depicts a diffusion barrier of 0.78 eV, higher than in the Ga-doped systems. The 0.25GaCe system has the lowest diffusion barrier, 0.55 eV, while the 0.50GaCe exhibits a diffusion barrier of 0.66 eV. Our calculations agree with the experimental measurements in which 0.25GaCe has the largest CO to CO₂ conversion (see Fig. 3). Although conversion increases in the 0.50GaCe and 0.75GaCe systems, the appearance of more O(I) bonds raises the diffusion barriers, reducing the CO to CO₂ oxidation reaction. The formation of the atomic-size channels due to Ga presence in the CeO₂ favors the bulk O(II) migration towards the surface to then interact with the CO molecules and induce the conversion to CO₂, a schematic representation of the O(II) migration (blue spheres) from the bulk to the surface is shown in Fig. 8a. Although 0.50GaCe has large Ga-O (II) bonds, compared to the 0.25GaCe system, which supposes a weak Ga-O interaction, we noticed that the 0.25GaCe has lower energy barrier, this could be explained since at the middle point of the oxygen diffusion the Ge-O bond distance is 1.98 and 1.96 Å for the 0.25GaCe and 0.50GaCe, respectively, which suggest a strong interaction and therefore a large energy barrier in the 0.50GaCe system. The ELF line profile corroborates this (Fig. 8c) since there is more electron population around the bond for the 0.50GaCe than 0.25GaCe.

Once we elucidate the diffusion process from the bulk to the surface, we want to understand the role of the Ga impregnation in the CeO₂(111) surface. Here we consider the O-terminated (111) surface because it is highly stable [73,74]. The surface model was constructed in a 2 × 2 periodicity considering that ¼ ML of Ga atoms is equivalent to the 0.25GaCe-IMP system. The surface comprises 11 at. layers (slab thickness of ~1 nm) and a vacuum space of ~3 nm to preclude surface self-interactions.

To evaluate the Ga impregnation, we adsorbed and incorporated Ga atoms on the O-terminated CeO₂(111) surface. Our surface stability

analysis demonstrated that Ga adsorption is unstable; instead, Ga atoms incorporate and take on Ce sites of the second surface layer (see Fig. S9b).

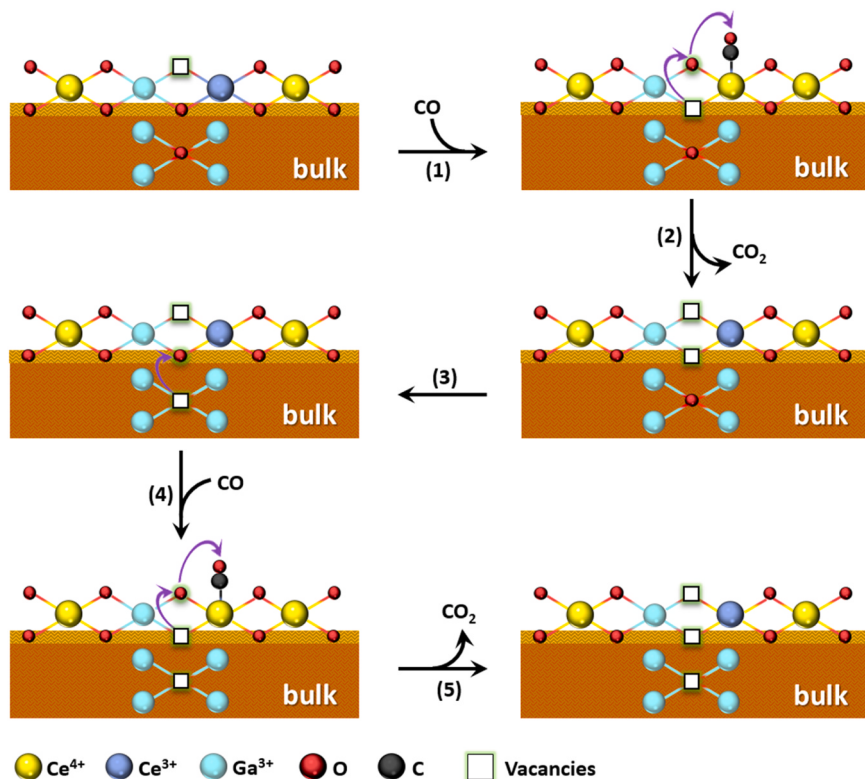
When incorporating Ga on the CeO₂ surface, structural changes also appear. The CeO₂ surface impregnated with Ga is shown in Fig. S10a. In Fig. S10b, the Ce-O bonding is depicted. Notice that the surface is very symmetric. Two kinds of bonds appear due to surface effects. First layer O-second layer Ce atoms are 0.01 Å larger than the ones formed by the second layer Ce and third layer O. In contrast, upon incorporating Ga atoms into the CeO₂ surface, larger structural changes appear. First, around the Ga atom, there are two types of bonds, just as in bulk. The ones more exposed to the surface, Ga-O(II), and the ones in the subsurface, Ga-O(I) bonds, see Fig. S10c. Also, the Ce-O bonds change, as evident in Fig. S10c. In this case, Ga generates larger structural arrangements than the surface effect. Interestingly, the Ga-O bonds at the surface elongate (from 2.35 Å in CeO₂ to 2.38 Å in the 0.25GaCe-IMP system) while the subsurface Ga-O bonds are reduced (from 2.36 Å in CeO₂ to 2.23 Å in the 0.25GaCe-IMP model). This Ga-induced effect is why surface O atoms tend to easily desorb from the surface to oxidize CO, leaving behind O vacancies that are further occupied by either the O atoms diffusing from the bulk (reaction in O₂ absence) or O₂ from the environment. In the last case, competition may exist between bulk O and O₂ from the environment, boosting the CO oxidation to CO₂.

To understand the process in a better way, we plotted the ELF for the pristine CeO₂ surface (Figs. S10d and S10e) and for the 0.25GaCe-IMP model (Figs. S10f and S10g). Upon comparing the ELF for both pristine and 0.25GaCe-IMP systems, it is evident that Ga has almost an absence of electrons, which indeed weakens the O bonds with their neighbors and improves the O desorption.

Once we explain why O desorbs from the surface, we now discuss why the 0.25GaCe system has a better performance than 0.25GaCe-IMP. In the former case, we hypothesize that Ga may be incorporating not just at the bulk but also at surface sites, and that explains why the activation energy is lower in 0.25GaCe than in the other cases. Remember that although there is more Ga content, the larger diffusion barrier from the bulk to the surface increases the activation temperature. A way to boost even more the CO₂ production rate is by combining the 0.25GaCe. The gallium incorporation in the cerium oxide plays an important role in oxygen activation.

3.5. Plausible mechanism for the catalysis of the CO oxidation on the 0.25GaCe sample

The data obtained in this work showed that the CO oxidation is enhanced over CeO₂-Ga₂O₃ mixed oxides than bare cerium oxide, specifically in the 0.25GaCe sample (Fig. 1), due to an improvement in the oxygen activation on this sample. A fast and efficient measure to evaluate the oxygen activation in our materials was the CO oxidation in O₂



Scheme 1. Plausible reaction route for CO oxidation without oxygen over the 0.25GaCe sample.

absence since the only source of oxygen atoms is the CeO₂ lattice, especially surface ones. The bare CeO₂ sample activates to transform CO to CO₂ in the temperature interval of 200–300 °C, in O₂ absence (Fig. 3). For the 0.25GaCe sample, CO₂ production was higher. Also, it occurred at lower temperatures (Fig. 3).

Our theoretical calculations suggest the Ga-O interaction is weaker than Ce-O (Fig. 7d); hence O donation from the CeO₂ lattice happens easily in the mixed oxides, as evidenced by dynamic OSC measurements (Table 2). Additionally, the DFT calculations indicated that Ga addition to CeO₂ improves the oxygen diffusion from the bulk to the surface due to the formation of atomic-size diffusion channels (Fig. 8).

In order to understand the effect Gallium on the oxygen activation on the cerium oxide the energy needed to supply oxygen via formation of vacancies for the CO oxidation, the energy needed to form the O_v formation was calculated. The formation of an oxygen vacancy (O_v) in the bare CeO₂ and 0.25GaCe materials was evaluated in a 2×2×2 supercell. The energy required to form the O_v was calculated following the equation:

$$E_{O_v} = E_{\text{reduced}} - E_{\text{stoichiometric}} - \frac{1}{2}n_o E_{O_2} \quad (2)$$

Where, E_{reduced} is the total energy of the system with an oxygen vacancy, E_{stoichiometric} is the energy reference that corresponds to the total energy of the system without vacancies, n_O is the deficit of O atoms in the system with respect to the reference, and E_{O₂} is the energy of an isolated O₂ molecule. Negative values evidence spontaneous vacancy formation and positive, an endothermic process.

The energy to form an O_v, in the bare CeO₂ material, is 3.64 eV, in agreement with other reports [21]. In the 0.25GaCe material two different sites for the O_v formation were considered: (i) O_v centered in the Ga atomic-size channels (Ga-O-Ga), and (ii) O_v centered between Ga and Ce atoms (Ga-O-Ce). In the first case, the O_v energy is –2.42 eV, and in the last case is –0.24 eV. Such results demonstrate that Ga incorporation boosts oxygen activation from the bulk to the surface through the Ga atomic-size channels and facilitates oxygen activation in

the neighborhood between Ga and Ce atoms.

Additionally, the formation of oxygen vacancies in bare CeO₂ and 0.25GaCe systems has been evaluated using the DFE formalism. The results are displayed in Fig. S11, considering Ga-rich conditions across the entire range of Ce chemical potential. According to the findings, the 0.25GaCe system (red line) exhibits stability, in comparison to bare CeO₂, under Ce-rich conditions from –0.25–0 eV; generating an oxygen vacancy leads to increased stability in the system. Various positions for the oxygen vacancy were considered: when the vacancy is placed within the Ga atomic size channel (Ga-O-Ga), close (Ga-O-Ga), and far (Ce-O-Ce) to them, corresponding to the green, blue, and magenta lines, respectively. The results indicate that the vacancies are thermodynamically stable, meaning they can spontaneously emerge in the systems, with the Ga-O-Ga vacancy being the most likely to be found. On the other hand, bare CeO₂ (black line) is stable in the chemical potential region from Ce-poor to Ce-intermediate conditions. Additionally, intrinsic oxygen vacancies are possible under Ce-poor conditions (gray line).

Based on our observations, we propose a plausible reaction route for CO oxidation without oxygen over the 0.25GaCe sample in Scheme 1. In the first step, the oxygen atom bonded to Ga in bulk is moved to the surface, where it can fill an oxygen vacancy located between Ga and Ce atoms (Scheme 1, step 1). In consequence, the Ce oxidation state changes from Ce⁺³ to Ce⁺⁴, which can act as an adsorption site for the CO_(g), forming adsorbed Ce⁺⁴-CO species (Scheme 1, step 1). This species can react with the active oxygen atom in the lattice to form CO_{2(g)} (Scheme 1, step 2). Therefore, the Ce⁺⁴ is reduced to Ce⁺³ (as demonstrated in the DRS-UV characterization, Fig. 2a). After that, a new oxygen vacancy on the surface is generated (Scheme 1, step 2), which can be refilled by oxygen atoms from the bulk (Scheme 1, steps 3 and 4). Again, the CO_(g) can be adsorbed on Ce⁺⁴ sites and then react with the surface active oxygen to produce CO_{2(g)} (Scheme 1, steps 4 and 5). The process described above repeats until the dynamic OSC oxygen is consumed (Table 2).

We have calculated the energy required to move an oxygen vacancy

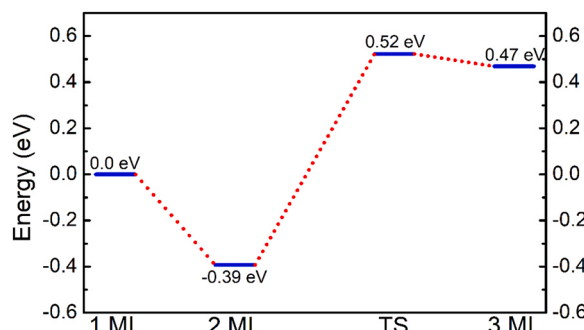


Fig. 9. Minimum energy pathway for O_v migration from surface to bulk.

from the surface to the inner layers through CI-NEB calculations, employing the surface model depicted in Fig. S10a. The minimum energy pathway for oxygen vacancy diffusion from the surface to the bulk is illustrated in Fig. 9. The energy reference corresponds to the oxygen vacancy located in the most exposed layer of the (111) surface (1 ML state). Upon formation of the oxygen vacancy on the surface, it rapidly migrates to a lower layer (2 ML state), resulting in an energy gain of 0.39 eV. This displacement causes an oxygen atom to move from the 2 ML to the 1 ML layer, facilitating oxygen migration from the inner layers to the surface. In Fig. 9, the TS state represents the activation energy required for the oxygen vacancy to move from the 2 ML to the 3 ML layer (3 ML state), which corresponds to an activation energy of 0.91 eV. The activation energy on the surface is similar to that obtained in the bulk (0.78 eV). Thus, we can conclude that the oxygen diffusion mechanism observed in the bulk is similar to that on the surface. The results indicate that oxygen atom diffusion from the bulk to the surface, through the displacement of an oxygen vacancy, is possible with an activation energy of 0.89 eV. This finding suggests that this proposed reaction mechanism is viable, as indicated by the findings presented in Fig. 9.

For CO oxidation in presence of O_2 , we propose a plausible reaction route that explains the catalysis of the CO oxidation over 0.25GaCe sample in Scheme 2, which focused mainly on the surface, due to the oxygen is supplied in the feed stream. In the first step the $CO_{(g)}$ is adsorbed on the Ce^{+3} sites as was evidenced by the appearance of the IR band at 2124 cm^{-1} (Fig. 6b), while the O_2 can be activated (dissociated) on the surface oxygen vacancies induced by the gallium atoms, in this way the $Ce^{+3}\text{-CO}$ can be readily transformed to $Ce^{+4}\text{-CO}$ species (Scheme 2, step 1) whose presence was proved by the IR band at 2174 cm^{-1} in the spectra obtained during CO and O_2 flow at increasing temperature (Fig. 6b). These species can react readily with the activated

oxygen to form $CO_{2(g)}$ (Scheme 2, step 2) in agreement with the results of catalytic activity and *operando* FTIR. Hence, Ce^{+4} sites would regenerate (from the oxidation of Ce^{+3}) and act as adsorption sites for another $CO_{(g)}$ molecule (Scheme 2, step 2 and 3). Thus, the formed $Ce^{+4}\text{-CO}$ species can react with the surface oxygen in the lattice to produce $CO_{2(g)}$ leading to an oxygen vacancy, in this manner the surface of the catalyst would completely restore the catalytic cycle (Scheme 2, step 4).

4. Conclusions

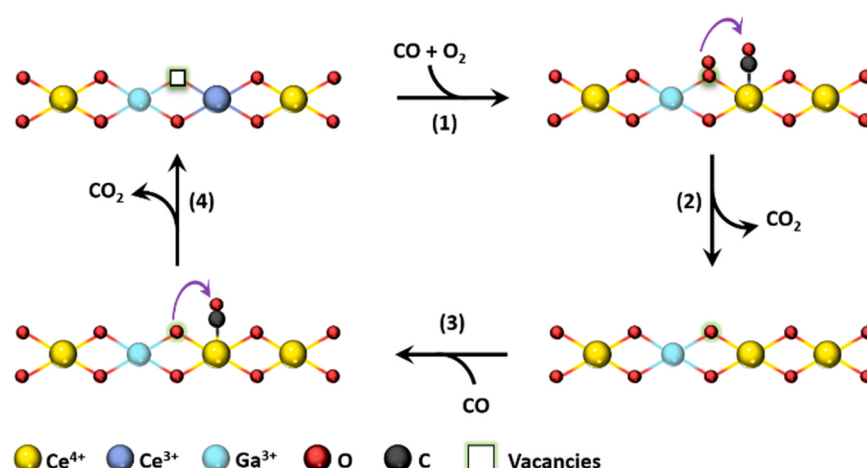
Our results highlights indicate that gallium incorporation in cerium-gallium oxide samples significantly promotes oxygen activation, which is a critical factor in determining their catalytic performance for CO oxidation. Both experimental findings and DFT simulations reveal that the presence of gallium in cerium oxide enhances oxygen activation and diffusion. Lower gallium contents promote oxygen activation, resulting in a higher CO oxidation. The generation of oxygen vacancies between Ga atoms and the formation of atomic-size channels that facilitate oxygen diffusion contribute to this improved performance. These insights can inform the optimization of synthesis processes and the development of more effective catalysts for CO oxidation, ultimately aiding environmental remediation efforts. Future research should continue to explore the precise mechanisms underlying the observed effects and investigate the potential of these materials for other selective oxidation reactions.

CRediT authorship contribution statement

Trino A. Zepeda designed the investigation, analyzed the data, and wrote the experimental section of the manuscript. **Sergio Fuentes** analyzed the data, discussed the results, and participated in writing the manuscript. **Alfredo Solis-Garcia** and **Sergio A. Gómez** conducted the experiments, analyzed the data, and participated in writing the manuscript. **Rodrigo Ponce-Pérez** and **Jonathan Guerrero-Sánchez** carried out the DFT calculations and analysis, provided helpful discussion and they wrote the theoretical section of the manuscript. All authors discussed the results.

Declaration of Competing Interest

The authors declare the following financial interests/personal relationships which may be considered as potential competing interests: Trino Zepeda reports financial support was provided by National Autonomous University of Mexico Center for Nanoscience and Nanotechnology.



Scheme 2. Plausible reaction route for CO oxidation over 0.25GaCe sample with oxygen supplied in the feed stream.

Data availability

Data will be made available on request.

Acknowledgements

We thank DGAPA-UNAM project IN112922, IN101523 and IA100822. Thanks to project CONACYT-F003 117373 for their partial financial support. Calculations were performed in the DGCTIC-UNAM Supercomputing Center projects, LANCAD-UNAM-DGTIC-422, LANCAD-UNAM-DGTIC-368 and LANCAD-UNAM-DGTIC-150. JGS acknowledges LNS-BUAP project 202201042N and THUBAT KAAL IPICYT supercomputing center project TKII-JGSA001 for their computational resources. The authors would like to thank Francisco Ruiz, David Dominguez, Eric Flores, J. Mendoza, Israel Gradilla, and Eloisa Aparicio for technical assistance.

Appendix A. Supporting information

Supplementary data associated with this article can be found in the online version at [doi:10.1016/j.apcatb.2023.122936](https://doi.org/10.1016/j.apcatb.2023.122936).

References

- [1] M. Rouhani, S. Kord, Z. Mirjafary, Ga-doped phagraphene as a superior media for sensing of carbon monoxide: a detailed theoretical investigation, *Phys. E* 116 (2020), 113710, <https://doi.org/10.1016/j.physe.2019.113710>.
- [2] N. Tit, K. Said, N.M. Mahmoud, S. Kouser, Z.H. Yamani, Ab-initio investigation of adsorption of CO and CO₂ molecules on graphene: role of intrinsic defects on gas sensing, *Appl. Surf. Sci.* 394 (2017) 219–230, <https://doi.org/10.1016/j.apsusc.2016.10.052>.
- [3] Y. Zhao, J. Hu, Z. Tan, T. Liu, W. Zeng, X. Li, C. Huang, S. Wang, Z. Huang, W. Ma, Ambient carbon monoxide and increased risk of daily hospital outpatient visits for respiratory diseases in Dongguan, China *Sci. Total Environ.* 668 (2019) 254–260, <https://doi.org/10.1016/j.scitotenv.2019.02.333>.
- [4] Z. Li, H. Wang, W. Zhao, X. Xu, Q. Jin, J. Qi, R. Yu, D. Wang, Enhanced catalytic activity of Au-CeO₂/Al₂O₃ monolith for low-temperature CO oxidation, *Catal. Commun.* 129 (2019), 105729, <https://doi.org/10.1016/j.catcom.2019.105729>.
- [5] S. Dey, G.C. Dhal, Materials progress in the control of CO and CO₂ emission at ambient conditions: an overview, *Mater. Sci. Energy Technol.* 2 (2019) 607–623, <https://doi.org/10.1016/j.mset.2019.06.004>.
- [6] J. Waikar, P. More, Oxygen deficient Ce doped CO supported on alumina catalyst for low-temperature CO oxidation in presence of H₂O and SO₂, *Fuel* 331 (2023) 12588, <https://doi.org/10.1016/j.fuel.2022.125880>.
- [7] X. Bi, Q. Zhang, K. Du, R. Yue, F. Wang, N. Li, Y. Huang Liu, Influence of pretreatment conditions on low-temperature CO oxidation over Pd supported UiO-66 catalysts, *Mol. Catal.* 509 (2021), 111633, <https://doi.org/10.1016/j.mcat.2021.111633>.
- [8] G.F. Zhou, J. Ma, S. Bai, L. Wang, Y. Guo, CO catalytic oxidation over Pd/CeO₂ with different chemical states of Pd, *Rare Met.* 39 (2020) 800–805, <https://doi.org/10.1007/s12598-019-01347-7>.
- [9] L.L. Lin, S.Y. Yao, R. Gao, X. Liang, Q.L. Yu, Y.C. Deng, J. Liu, M. Peng, Z. Jiang, S. Li, Y.-W. Li, X.-D. Wen, W. Zhou, D. Ma, A highly CO-tolerant atomically dispersed Pt catalyst for chemoselective hydrogenation, *Nat. Nanotechnol.* 14 (2019) 354–361, <https://doi.org/10.1038/s41565-019-0366-5>.
- [10] Z. Zhou, S. Kool, M. Flytzani-Stephanopoulos, H. Saltsburg, The role of the interface in CO oxidation on Au/CeO₂ multilayer nanotowers, *Adv. Funct. Mater.* 18 (2008) 2801–2807, <https://doi.org/10.1002/adfm.200800025>.
- [11] Y. Zhang, B. Zhaorigetu, M. Jia, C. Chen, J. Zhao, Clay-based SiO₂ as active support of gold nanoparticles for CO oxidation catalyst: pivotal role of residual Al, *Catal. Commun.* 35 (2013) 72–75, <https://doi.org/10.1016/j.catcom.2013.02.006>.
- [12] E.V. Abkhalimov, O.A. Boeva, A.A. Odintsov, R.D. Solovov, K.N. Zhavoronkova, B. G. Ershov, The H₂-D₂ exchange reaction catalyzed by gold nanoparticles supported on γ -Al₂O₃: effect of particle size on the reaction rate, *Catal. Commun.* 133 (2020), 105840, <https://doi.org/10.1016/j.catcom.2019.105840>.
- [13] J.C. Fierro-Gonzalez, B.C. Gates, Mononuclear Au^{III} and Au^I complexes bonded to zeolite NaY: catalysts for CO oxidation at 298 K, *J. Phys. Chem. B* 108 (2004) 16999–17002, <https://doi.org/10.1021/jp046171y>.
- [14] J.M. Zamaro, A.V. Boix, A. Martínez-Hernández, CO oxidation over Au supported on Mn-ZSM5 and Mn-MOR, *Catal. Commun.* 69 (2015) 212–216, <https://doi.org/10.1016/j.catcom.2015.06.018>.
- [15] M. Haruta, S. Tsubota, T. Kobayashi, H. Kageyama, M.J. Genet, B. Delmon, Low-temperature oxidation of CO over gold supported on TiO₂, α -Fe₂O₃, and Co₃O₄, *J. Catal.* 144 (1993) 175–192, <https://doi.org/10.1006/jcat.1993.1322>.
- [16] J.L. Vincent, P.A. Crozier, Atomic level fluxional behavior and activity of CeO₂-supported Pt catalysts for CO oxidation, *Nat. Commun.* 12 (2021) 5789, <https://doi.org/10.1038/s41467-021-26047-8>.
- [17] A. Trovarelli, C.D. Leitenburg, G. Dolcetti, Design better cerium-based oxidation catalysts, *ChemTech* 27 (1997) 32–37.
- [18] P. Li, X. Chen, Y. Li, J.W. Schwank, A review on oxygen storage capacity of CeO₂-based materials: influence factors, measurement techniques, and applications in reactions related to catalytic automotive emissions control, *Catal. Today* 327 (2019) 90–115, <https://doi.org/10.1016/j.cattod.2018.05.059>.
- [19] W. Deng, M. Flytzani-Stephanopoulos, On the issue of the deactivation of Au–ceria and Pt–ceria water–gas shift catalysts in practical fuel-cell applications, *Angew. Chem. Int. Ed.* 45 (2006) 2285–2289, <https://doi.org/10.1002/anie.200503220>.
- [20] J. Vecchietti, S. Collins, J.J. Delgado, M.M. Eloy del Rio, X. Chen, S. Bernal, A. Bonivardi, Gold catalysts supported on cerium–gallium mixed oxide for the carbon monoxide oxidation and water gas shift reaction, *Top. Catal.* 54 (2011) 201–209, <https://doi.org/10.1007/s11244-011-9653-6>.
- [21] J. Vecchietti, S. Collins, W. Xu, L. Barrio, D. Stacchiola, M. Calatayud, F. Tielens, J. J. Delgado, A. Bonivardi, Surface reduction mechanism of cerium–gallium mixed oxides with enhanced redox properties, *J. Phys. Chem. C* 117 (2013) 8822–8831.
- [22] L. Xu, W.-Q. Huang, L.-L. Wang, G.-F. Huang, Interfacial interactions of semiconductor with graphene and reduced graphene oxide: CeO₂ as a case study, *ACS Appl. Mater. Interfaces* 6 (2014) 20350–20357, <https://doi.org/10.1021/am505877z>.
- [23] N. Yao, R. Meng, F. Wu, Z. Fan, G. Cheng, W. Luo, Oxygen-vacancy-induced CeO₂/Co₄O heterostructures toward enhanced pH-universal hydrogen evolution reactions, *Appl. Catal., B, Environ.* 277 (2020), 119282, <https://doi.org/10.1016/j.apcatb.2020.119282>.
- [24] Y. Feng, Q. Wan, H. Xiong, S. Zhou, X. Chen, X.I. Pereira-Hernandez, Y. Wang, S. Lin, A.K. Datye, H. Guo, Correlating DFT calculations with CO oxidation reactivity on Ga-doped Pt/CeO₂ single-atom catalysts, *J. Phys. Chem. C* 122 (2018) 22460–22468, <https://doi.org/10.1021/acs.jpcc.8b05815>.
- [25] S. Tang, L. Xu, B. Peng, F. Xiong, T. Chen, X. Luo, X. Huang, H. Li, J. Zeng, Z. Ma, Ling-Ling Wang, Ga-doped Pd/CeO₂ model catalysts for CO oxidation reactivity: a density functional theory study, *Appl. Surf. Sci.* 575 (2022), 151655, <https://doi.org/10.1016/j.apsusc.2021.151655>.
- [26] T. Wang, F. Jiang, G. Liu, L. Zeng, Z.-jian Zhao, J. Gong, Effects of Ga doping on Pt/CeO₂-Al2O₃ catalysts for propane dehydrogenation, *AIChE J.* 62 (2016) 4365–4376, <https://doi.org/10.1002/aic.15339>.
- [27] J. Vecchietti, P. Lustemberg, E.L. Fornero, M. Calatayud, S.E. Collins, S. Mohr, M. V. Ganduglia-Pirovano, J. Libuda, A.L. Bonivardi, Controlled selectivity for ethanol steam reforming reaction over doped CeO₂ surfaces: the role of gallium, *Appl. Catal. B, Environ.* 277 (2020), 119103, <https://doi.org/10.1016/j.apcatb.2020.119103>.
- [28] K.J. Caulfield, R. Cooper, J.F. Boas, Luminescence from electron-irradiated sapphire, *Phys. Rev. B* 47 (1993) 55–61, <https://doi.org/10.1103/PhysRevB.47.55>.
- [29] G. Kresse, J. Hafner, Ab initio molecular-dynamics simulation of the liquid-metal–amorphous–semiconductor transition in germanium, *Phys. Rev. B* 49 (1994) 14251–14269, <https://doi.org/10.1103/PhysRevB.49.14251>.
- [30] G. Kresse, J. Furthmüller, Efficiency of ab-initio total energy calculations for metals and semiconductors using a plane-wave basis set, *Comput. Mater. Sci.* 6 (1996) 15–50, [https://doi.org/10.1016/0927-0256\(96\)00008-0](https://doi.org/10.1016/0927-0256(96)00008-0).
- [31] G. Kresse, J. Furthmüller, Efficient iterative schemes for ab initio total-energy calculations using a plane-wave basis set, *Phys. Rev. B* 54 (1996) 11169–11186, <https://doi.org/10.1103/PhysRevB.54.11169>.
- [32] P.E. Blöchl, Projector augmented-wave method, *Phys. Rev. B* 50 (1994) 17953–17979, <https://doi.org/10.1103/PhysRevB.50.17953>.
- [33] G. Kresse, D. Joubert, From ultrasoft pseudopotentials to the projector augmented-wave method, *Phys. Rev. B* 59 (1999) 1758–1775, <https://doi.org/10.1103/PhysRevB.59.1758>.
- [34] J.P. Perdew, K. Burke, M. Ernzerhof, Generalized gradient approximation made simple, *Phys. Rev. Lett.* 77 (1996) 3865–3868, <https://doi.org/10.1103/PhysRevLett.77.3865>.
- [35] S. Grimme, J. Antony, S. Ehrlich, H. Krieg, A consistent and accurate ab initio parametrization of density functional dispersion correction (DFT-D) for the 94 elements H–Pu, *J. Chem. Phys.* 132 (2010) 1–19, <https://doi.org/10.1063/1.3382344>.
- [36] S. Grimme, S. Ehrlich, L. Goerigk, Effect of the damping function in dispersion corrected density functional theory, *J. Comput. Chem.* 32 (2011) 1211–1491, <https://doi.org/10.1002/jcc.21759>.
- [37] M.G. Moreno-Armenta, J. Guerrero-Sánchez, S.J. Gutiérrez-Ojeda, H.N. Fernández-Escamilla, D.M. Hoat, R. Ponce-Pérez, Theoretical investigation of the MXene precursors Mo_xV_{4-x}AlC₃ (0 ≤ x ≤ 4), *Sci. Rep.* 13 (2023) 3271, <https://doi.org/10.1038/s41598-023-30443-z>.
- [38] R. Ponce-Pérez, M.G. Moreno-Armenta, J. Guerrero-Sánchez, Selective incorporation of Fe and Co into the Ni₂MnGa (001) surfaces: a DFT analysis, *Surf. Interfaces* 34 (2022), 102367, <https://doi.org/10.1016/j.surfin.2022.102367>.
- [39] J.R. Rodriguez, C. Belman, S.B. Aguirre, A. Simakov, S.A. Aguilera, R. Ponce-Pérez, J. Guerrero-Sánchez, M.G. Moreno, D. Saucedo, V.G. Pol, Reversible lithium-ion storage in H₂Bi₃Ge₃O₉-based anode: experimental and theoretical studies, *J. Electroanal. Chem.* 923 (2022), 116804, <https://doi.org/10.1016/j.jelechem.2022.116804>.
- [40] H.J. Monkhorst, J.D. Pack, Special points for Brillouin-zone integrations, *Phys. Rev. B* 13 (1976) 5188–5192, <https://doi.org/10.1103/PhysRevB.13.5188>.
- [41] G. Henkelman, A climbing image nudged elastic band method for finding saddle points and minimum energy paths, *J. Chem. Phys.* 113 (2000) 9901–9904, <https://doi.org/10.1063/1.1329672>.
- [42] G. Henkelman, H. Jónsson, Improved tangent estimate in the nudged elastic band method for finding minimum energy paths and saddle points, *J. Chem. Phys.* 113 (2000) 9978–9985, <https://doi.org/10.1063/1.1323224>.

- [43] J.A. Hernandez, S.A. Gómez, T.A. Zepeda, J.C. Fierro-González, G.A. Fuentes, Insight into the Deactivation of Au/CeO₂ Catalysts Studied by In Situ Spectroscopy during the CO-PROX Reaction, *ACS Catal.* 5 (2015) 4003–4012, <https://doi.org/10.1021/acscatal.5b00739>.
- [44] A. Sharma, M. Varshney, H. Saraswat, S. Chaudhary, J. Parkash, H.-J. Shin, K.-H. Chae, S.-O. Won, Nano-structured phases of gallium oxide (GaOOH, α -Ga₂O₃, β -Ga₂O₃, γ -Ga₂O₃, δ -Ga₂O₃, and ϵ -Ga₂O₃): fabrication, structural, and electronic structure investigations, *Int. Nano Lett.* 10 (2020) 71–79, <https://doi.org/10.1007/s40089-020-00295-w>.
- [45] J. Li, T. Xia, J. Xu, C. Zhang, L. Xu, Z. Wu, S. Yao, Boosting the plasma catalytic performance of CeO₂/ γ -Al₂O₃ in long-chain alkane VOCs via tuning the crystallite size, *Appl. Surf. Sci.* 611 (2023), 155742, <https://doi.org/10.1016/j.apsusc.2022.155742>.
- [46] J.L.F. Da Silva, Stability of the Ce₂O₃ phases: a DFT+U investigation, *Phys. Rev.* 76 (2007), 193108, <https://doi.org/10.1103/PhysRevB.76.193108>.
- [47] W. Deng, J. de Jesús, H. Saltsburg, M. Flytzani-Stephanopoulos, Low-content gold-ceria catalysts for the water-gas shift and preferential CO oxidation reactions, *Appl. Catal. A Gen.* 291 (2005) 126–135, <https://doi.org/10.1016/j.apcata.2005.02.048>.
- [48] F. Fu, H. Saltsburg, M. Flytzani-Stephanopoulos, Active nonmetallic Au and Pt species on ceria-based water-gas shift catalysts, *Science* 301 (2003) 935–938, <https://doi.org/10.1126/science.1085721>.
- [49] A. Trovarelli, Catalytic properties of ceria and CeO₂-containing materials, *Catal. Rev. Sci. Eng.* 38 (1999) 439–520, <https://doi.org/10.1080/01614949608006464>.
- [50] E. Gonzalez-A, R. Rangel, A. Solís-García, A.M. Venecia, T.A. Zepeda, FTIR investigation under reaction conditions during CO oxidation over Ru(x)-CeO₂ catalysts, *Mol. Catal.* 493 (2020), 111086, <https://doi.org/10.1016/j.mcat.2020.111086>.
- [51] B. Liu, W. Yang, J. Li, X. Zhang, P. Niu, X. Jiang, Template approach to crystalline GaN nanosheets, *Nano Lett.* 17 (2017) 3195–3201, <https://doi.org/10.1021/acs.nanolett.7b00754>.
- [52] J.A. Odriozola, M. Montes, L.M. Gandía, Selective CO removal over Au/CeFe and CeCu catalysts in microreactors studied through kinetic analysis and CFD simulations, *Chem. Eng. J.* 167 (2011) 588–596, <https://doi.org/10.1016/j.cej.2010.08.083>.
- [53] C.-T. Shao, W.-Z. Lang, X. Yan, Y.-J. Guo, Catalytic performance of gallium oxide based-catalysts for the propane dehydrogenation reaction: effects of support and loading amount, *RSC Adv.* 7 (2017) 4710–4723, <https://doi.org/10.1039/C6RA27204E>.
- [54] B. Wang, B. Chen, Y. Sun, H. Xiao, X. Xu, M. Fu, J. Wu, L. Chen, D. Ye, Effects of dielectric barrier discharge plasma on the catalytic activity of Pt/CeO₂ catalysts, *Appl. Catal. B Environ.* 238 (2018) 328–338, <https://doi.org/10.1016/j.apcatab.2018.07.044>.
- [55] F. Huang, C. Chen, F. Wang, B. Wang, L. Zhang, S. Lu, K. Li, Effect of calcination temperature on the catalytic oxidation of formaldehyde over Co₃O₄-CeO₂ catalysts, *Catal. Surv. Asia.* 21 (2017) 143–149, <https://doi.org/10.1007/s10563-017-9234-1>.
- [56] C. Xu, Y. Wu, S. Li, J. Zhou, J. Chen, M. Jiang, H. Zhao, G. Qin, Engineering the epitaxial interface of Pt-CeO₂ by surface redox reaction guided nucleation for low temperature CO oxidation, *J. Mater. Sci. Technol.* 40 (2020) 39–46, <https://doi.org/10.1016/j.jmst.2019.08.036>.
- [57] X. Wang, D. Liu, J. Li, J. Zhen, H. Zhang, Clean synthesis of Cu₂O@CeO₂ core@shell nanocubes with highly active interface, *NPG Asia Mater.* 7 (2015), e158, <https://doi.org/10.1038/am.2014.128>.
- [58] R. Körner, M. Ricken, J. Nöltig, Phase transformations in reduced ceria: determination by thermal expansion measurements, *J. Solid. State Chem.* 78 (1989) 136–147, [https://doi.org/10.1016/0022-4596\(89\)90137-0](https://doi.org/10.1016/0022-4596(89)90137-0).
- [59] K. Krishna, A. Bueno-López, M. Makkee, J.A. Moulijn, Potential rare earth modified CeO₂ catalysts for soot oxidation, *Appl. Catal. B Environ.* 75 (2007) 189–200, <https://doi.org/10.1016/j.apcatab.2007.04.010>.
- [60] A. Bueno-López, Diesel soot combustion ceria catalysts, *Appl. Catal. B Environ.* 146 (2014) 1–11, <https://doi.org/10.1016/j.apcatab.2013.02.033>.
- [61] R. Ran, J. Fan, D. Weng, Microstructure and oxygen storage capacity of Sr-modified Pt/CeO₂-ZrO₂ catalysts, *Prog. Nat. Sci.* 22 (2012) 7–14, <https://doi.org/10.1016/j.pnsc.2011.12.002>.
- [62] Q. Liang, X. Wu, X. Wu, D. Weng, Role of surface area in oxygen storage capacity of ceria-zirconia as soot combustion catalyst, *Catal. Lett.* 119 (2007) 265–270, <https://doi.org/10.1007/s10562-007-9228-0>.
- [63] M. Boaro, F. Giordano, S. Recchia, V.D. Santo, M. Giona, A. Trovarelli, On the mechanism of fast oxygen storage and release in ceria-zirconia model catalysts, *Appl. Catal. B Environ.* 52 (2004) 225–237, <https://doi.org/10.1016/j.apcatab.2004.03.021>.
- [64] D. Duprez, C. Descorme, T. Birchem, E. Rohart, Oxygen storage and mobility on model three-way catalysts, *Top. Catal.* 16 (2001) 49–56, <https://doi.org/10.1023/A:1016622612521>.
- [65] N. Hickey, P. Fornasiero, R.D. Monte, J. Kašpar, M. Graziani, G. Dolcetti, A comparative study of oxygen storage capacity over Ce_{0.6}Zr_{0.4}O₂ mixed oxides investigated by temperature-programmed reduction and dynamic OSC measurements, *Catal. Lett.* 72 (2001) 45–50, <https://doi.org/10.1023/A:1009096106758>.
- [66] G. Jacobs, R.A. Keogh, B.H. Davis, Steam reforming of ethanol over Pt/cevia with co-fed hydrogen, *J. Catal.* 245 (2007) 326–337, <https://doi.org/10.1016/j.jcat.2006.10.018>.
- [67] B. Liu, C. Li, G. Zhang, X. Yao, S.S.C. Chuang, Z. Li, Oxygen vacancy promoting dimethyl carbonate synthesis from CO₂ and methanol over Zr-doped CeO₂ nanorods, *ACS Catal.* 8 (2018) 10446–10456, <https://doi.org/10.1021/ascat.8b00415>.
- [68] Z. Wu, M. Li, S.H. Overbury, On the structure dependence of CO oxidation over CeO₂ nanocrystals with well-defined surface planes, *J. Catal.* 285 (2012) 61–73, <https://doi.org/10.1016/j.jcat.2011.09.011>.
- [69] M. Daturi, C. Binet, J.C. Lavalle, G. Blanchard, Surface FTIR investigations on Ce_xZr_{1-x}O₂ system, *Surf. Interface Anal.* 30 (2000) 273–277, [https://doi.org/10.1002/1096-9918\(200008\)30:1<273::AID-SIA715>3.0.CO;2-G](https://doi.org/10.1002/1096-9918(200008)30:1<273::AID-SIA715>3.0.CO;2-G).
- [70] G.-X. Qian, R.M. Martin, D.J. Chadi, First-principles study of the atomic reconstructions and energies of Ga- and As-stabilized GaAs(100) surfaces, *Phys. Rev. B* 38 (1988) 7649–7663, <https://doi.org/10.1103/PhysRevB.38.7649>.
- [71] J.C. Moreno H, R. Ponce-Pérez, G.H. Cocoletzi, N. Takeuchi, Antiferromagnetic coupling in the initial stages of the MnN epitaxial growth on the CrN (0 0 1) surface, *Appl. Surf. Sci.* 573 (2022), 151451, <https://doi.org/10.1016/j.apsusc.2021.151451>.
- [72] J.C. Moreno Hernández, R. Ponce-Pérez, G. Hernández Cocoletzi, D. Minh Hoat, N. Takeuchi, Tuning the half-metallicity in reconstructed CrN (111) surfaces, *Surf. Interfaces* 35 (2022), 102420, <https://doi.org/10.1016/j.surfin.2022.102420>.
- [73] Y. Lin, Z. Wu, J. Wen, K.R. Poepelmeier, L.D. Marks, Imaging the atomic surface structures of CeO₂ nanoparticles, *Nano Lett.* 14 (2014) 191–196, <https://doi.org/10.1021/nl403713b>.
- [74] Z. Wu, M. Li, D.R. Mullins, S.H. Overbury, Probing the surface sites of CeO₂ nanocrystals with well-defined surface planes via methanol adsorption and desorption, *ACS Catal.* 2 (2012) 2224–2234, <https://doi.org/10.1021/cs300467p>.